Pressure-based large-eddy simulation of under-expanded hydrogen jets for engine applications

INTERNATIONAL JOURNAL OF HYDROGEN ENERGY 49 (2024) 771–783

Available online at www.sciencedirect.com

ScienceDirect

journal homepage: www.elsevier.com/locate/he

Pressure-based large-eddy simulation of under-expanded hydrogen jets for engine applications

A. Ballatore*, J.A. van Oijen

Eindhoven University of Technology, Department of Mechanical Engineering, Power & Flow, Building 15, Groene Loper 5, 5612 AE, Eindhoven, the Netherlands

HIGHLIGHTS

- Our model correctly describes the mixing of H2 jets for DI-CI engine applications.
- Pressure-based solvers can be used with reasonable accuracy for under-expanded flows.
- Under-relaxation factors help such p-based algorithm improving the shock resolution.
- The WALE model with 4th-order cubic convective schemes delivers the most accurate results.

ARTICLE INFO

Article history:
Received 26 June 2023
Received in revised form
31 August 2023
Accepted 6 September 2023
Available online 22 September 2023

Keywords:
Under-expanded jets
Large-eddy simulation
Pressure-based
OpenFOAM
Compressible effects

ABSTRACT

An assessment of Large-Eddy Simulations (LES) of non-reactive under-expanded hydrogen jets by using a pressure-based algorithm is presented. Such jets feature strong compressible discontinuities often considered to be best dealt with by a density-based solver. The crucial contribution of this work is to evaluate the suitability of the pressure-based solver to correctly describe the flow field of gaseous hydrogen jets for engine applications, despite the presence of shock waves in the under-expanded near-orifice region. Inherently, the paper aims at providing guidance on the corresponding numerical aspects to simulate these flows. Hydrogen jets in an argon atmosphere at three different injection pressures are simulated and the results are compared to experiments in literature. Jet tip penetration and cone angle are the main investigated parameters. A good match is found, confirming the solidity of the proposed model. Different LES sub-grid scale models and discretisation schemes are then investigated in order to find the best approach in terms of accuracy and required computational cost. In particular, it is found that the WALE model coupled with a 4th-order cubic scheme for the convective terms yields the most suitable configuration.

* *Corresponding author.*
E-mail address: a.ballatore@tue.nl (A. Ballatore).

https://doi.org/10.1016/j.ijhydene.2023.09.062

1. Introduction

Hydrogen has been labeled for a long time as the fuel of the future [1–4], due to its carbon-free combustion and the ability to achieve high energy efficiency. Moreover, it can be produced from renewable energy sources, enabling efficient large-scale storage and transport of renewable energy. The unique thermo-physical properties of hydrogen can facilitate the design of a highly efficient internal combustion engine (ICE) [5]. The high diffusivity of hydrogen, for instance, may enhance in-cylinder fuel-air mixing. Furthermore, the wide flammability limit from 4 to 76 vol% hydrogen in air, alongside with the high flame speed, indicates that hydrogen ICE can operate considerably lean, thus improving thermal efficiency [6–9]. In particular, direct injection of hydrogen, aside from enabling high volumetric efficiency, avoids possibly undesired combustion-related phenomena such as engine knock [10,11]. However, due to its low density, H_2 requires high injection pressures to fully penetrate in the cylinder [12]. This typically leads to a turbulent under-expanded jet, as explained in the following.

Let us consider a converging nozzle, like the ones normally involved in engine applications. With respect to the pressure profiles shown in Fig. 1, the most trivial case is when the injection pressure P_0 and the ambient pressure P_∞ are the same. In this case (curve a), there is no flow. When the ratio between the total pressure in the nozzle P_0 and the ambient pressure P_∞, namely the Nozzle Pressure Ratio (NPR), increases, the flow becomes subsonic. This trend (curve b) holds until the outlet velocity reaches sonic conditions, i.e. the Mach number is $Ma = 1$ (curve c). The exit pressure P_e and the ambient pressure are still equal, and the flow is said to be choked. The value of NPR where this chocked condition occurs, is labeled as the critical pressure ratio. Increasing the injection pressure further will not have any additional effect on the flow velocity within the nozzle, as the maximum Mach number in the minimum-area section is 1. The local speed of sound c will also remain the same at the exit. In fact, $c = \sqrt{\gamma R T_e}$, with γ being the specific heat ratio, R the specific gas constant and T_e the exit temperature. For an ideal gas, T_e, at fixed γ and Ma, depends solely on the injection temperature T_0, that is kept fixed when increasing the injection pressure P_0. If the injection pressure P_0 increases further, an under-expanded condition occurs (curve d). At first, this is *moderately* under-expanded: the outlet velocity cannot go beyond $Ma = 1$, and so the exit pressure becomes higher than the ambient one; as a consequence, a further expansion occurs in the near-orifice region, in order to let the pressure reduce to the ambient one. A very weak normal shock forms at the exit of the nozzle, together with a pattern of oblique reflected shock waves. As P_0 is further increased, the flow reaches a point where eventually it becomes *highly* under-expanded: at the nozzle exit, an infinite number of rarefaction waves (the so-called Prandtl-Mayer fan) spreads onto the jet boundary and collapse into a slightly-curved oblique shock wave named Mach disk.

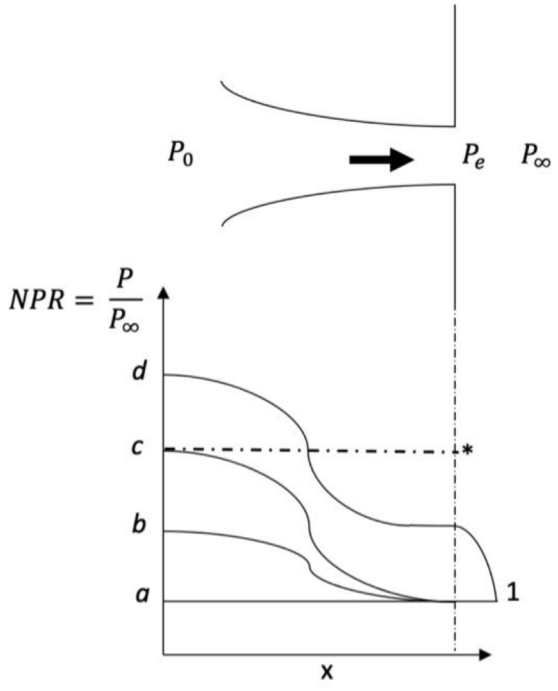

Fig. 1 – Schematic pressure distributions in a converging nozzle.

In-depth understanding of both the aforementioned under-expansion process and the related turbulent mixing past the nozzle orifice is therefore required for the design of an efficient gaseous injection system and for the analysis of the most suitable associated injection strategies aimed at better mixture quality and clean combustion [13], by improving the jet penetration and the mixing of the fuel with the surrounding environment.

From a computational point of view, the near-nozzle region is the most challenging aspect in an under-expanded flow. It has mostly been studied using density-based solvers, in which the primitive variable is the density, directly computed from mass conservation with pressure being updated through an equation of state. For instance, Hamzehloo [13], Vuorinen et al. [14], and Li et al. [15] used a density-based approach to tackle, by means of LES, the resolution of the shock cells pattern of the near-nozzle region. Duronio et al. [16] and Bonelli et al. [17] did the same but with RANS (Reynolds-averaged Navier Stokes) simulations. While this is the most natural approach for the resolution of shock waves, since the governing equations are solved for the conservative variables, density-based solvers on the other hand experience stiffness problems as well as a loss of accuracy when approaching the low Mach number limit. Moreover, the time step is limited by the most rapidly propagating wave, which becomes restrictive for low Mach number flows [18]. Lai et al. [19] showed, in RANS, the performance of the pressure-based numerical method to resolve shocks and other discontinuities to rival those of the density-based methods. Moreover, in injection for ICE where the flow in the largest part of the computational domain is at a low Mach number but in some parts supersonic flow exists, a pressure-based solver may be an attractive as well as efficient choice [20]. For instance, Li et al. [21] investigated under-expanded hydrogen jets with RANS by first computing the near-nozzle flow field in a smaller domain using a density-based solver, and then use that

solution to compute the flow further downstream through a pressure-based solver. Babayev et al. [22] conducted their computational study by means of a pressure-based PISO algorithm coupled with RANS modelling to assess the characteristics of a H_2 direct-injection compression-ignition combustion concept.

In H_2-ICE, the aforementioned supersonic region covers indeed only a small part of the domain, and the main focus is correctly describing the fuel/oxidizer mixing on a larger scale, the whole combustion chamber, in view of an engine application. Solving the largest turbulent structures, rather than time-averaging like in RANS, helps capturing accurately this phenomenon, hence the use of LES is crucial [23]. Moreover, the mixing process occurs mostly downstream of the under-expanded region, where the local Mach number is low and the flow can be deemed incompressible, and where consequently density-based solver could fail in accuracy and efficiency. Therefore, we aim to study for the first time such under-expanded jets with LES through a pressure-based solver, and compare the results against experimental literature to validate such an approach. In the next sections, after a brief review of the mathematical background of the problem, the computational setup will be introduced, and the results will be discussed.

2. Numerical problem

The dynamics of a fluid is governed by mass, momentum, and energy conservation, namely the (compressible) Navier-Stokes equations. For a non-reactive flow they read [24]:

$$\frac{\partial \rho}{\partial t} + \frac{\partial}{\partial x_i}(\rho u_i) = 0 \tag{1}$$

$$\frac{\partial (\rho u_j)}{\partial t} + \frac{\partial}{\partial x_i}(\rho u_i u_j) = -\frac{\partial p}{\partial x_j} + \frac{\partial \tau_{ij}}{\partial x_i} \tag{2}$$

$$\frac{\partial \rho h_s}{\partial t} + \frac{\partial}{\partial x_i}(\rho u_i h_s) = \frac{Dp}{Dt} + \frac{\partial}{\partial x_i}\left(\lambda \frac{\partial T}{\partial x_i}\right) + \tau_{ij}\frac{\partial u_i}{\partial x_j} - \frac{\partial}{\partial x_i}\left(\rho \sum_{k=1}^{N} V_{k,i} Y_k h_{s,k}\right) + \dot{\omega}_T \tag{3}$$

with:

$$\frac{Dp}{Dt} = \frac{\partial p}{\partial t} + u_i \frac{\partial p}{\partial x_i}, \tag{4}$$

where ρ is the density, u_i the ith component of the velocity vector, p the pressure, h_s is the sensible enthalpy, $V_{k,i}$ is the diffusion velocity of the ith species, $q_i = -\lambda \frac{\partial T}{\partial x_i}$ is the heat flux vector, with T the fluid temperature and λ the thermal conductivity. The chemical heat release rate $\dot{\omega}_T$ is zero for the non-reacting flows considered in this work. The total stress tensor τ_{ij} is given by:

$$\tau_{ij} = \mu\left[\frac{\partial u_i}{\partial x_j} + \frac{\partial u_j}{\partial x_i}\right] - \left(\frac{2}{3}\mu \frac{\partial u_k}{\partial x_k}\right)\delta_{ij}, \tag{5}$$

with δ_{ij} the Kronecker delta. If the fluid is assumed to be an ideal gas (acceptable assumption for hydrogen jets [25]), then pressure and density can be linked by the well-known ideal gas law $p = \rho RT$, with R being the specific gas constant. In total, five equations are needed: one for the density, three for the components of the velocity, one for the energy.

If the gas consists of more than one species, then another set of transport equations adds up to the five above, namely:

$$\frac{\partial \rho Y_k}{\partial t} + \frac{\partial}{\partial x_i}(\rho u_i Y_k) = \frac{\partial}{\partial x_i}\left(\rho D_k \frac{\partial Y_k}{\partial x_i}\right) + \dot{\omega}_k, \tag{6}$$

where Y_k indicates the mass fraction of species $k = 1, \ldots, N$, D_k the corresponding molecular diffusion coefficient, and ω_k the net chemical production rate, which is null for the non-reactive flows considered in this study. Since for the conservation of mass, the sum of all the species fractions must be equal to 1, these transport equations constitute $N - 1$ additional relations to be solved together with the aforementioned five.

2.1. LES modelling

Denoting Reynolds-averaged quantities by a bar $\overline{f}$ and Favre-averaged quantities by a tilde $\widetilde{f} = \overline{\rho f}/\overline{\rho}$, the filtered compressible Navier-Stokes equations can be written as [24]:

$$\frac{\partial \overline{\rho}}{\partial t} + \frac{\partial}{\partial x_i}(\overline{\rho}\widetilde{u}_i) = 0 \tag{7}$$

$$\frac{\partial}{\partial t}(\overline{\rho}\widetilde{u}_i) + \frac{\partial}{\partial x_i}(\overline{\rho}\widetilde{u}_i\widetilde{u}_j) = -\frac{\partial \overline{p}}{\partial x_j} + \frac{\partial}{\partial x_i}[\overline{\tau}_{ij} - \overline{\rho}(\widetilde{u_i u_j} - \widetilde{u}_i\widetilde{u}_j)] \tag{8}$$

$$\frac{\partial \overline{\rho}\widetilde{h}_s}{\partial t} + \frac{\partial}{\partial x_i}(\overline{\rho}\,\widetilde{u}_i\widetilde{h}_s) = \frac{\overline{Dp}}{Dt} + \frac{\partial}{\partial x_i}\left[\lambda\overline{\frac{\partial T}{\partial x_i}} - \overline{\rho}(\widetilde{u_i h_s} - \widetilde{u}_i\widetilde{h}_s)\right] + \overline{\tau_{ij}\frac{\partial u_i}{\partial x_j}} - \frac{\partial}{\partial x_i}\left(\overline{\rho\sum_{k=1}^{N} V_{k,i}Y_k h_{s,k}}\right) + \overline{\dot{\omega}_T} \tag{9}$$

$$\frac{\partial(\overline{\rho}\widetilde{Y_k})}{\partial t} + \frac{\partial}{\partial x_i}(\overline{\rho}\widetilde{u}_i\widetilde{Y_k}) = \frac{\partial}{\partial x_i}\left[\overline{V_{k,i}Y_k} - \overline{\rho}(\widetilde{u_i Y_k} - \widetilde{u}_i\widetilde{Y_k})\right] + \overline{\dot{\omega}_k} \tag{10}$$

where

$$\frac{\overline{Dp}}{Dt} = \frac{\partial \overline{p}}{\partial t} + \overline{u_i\frac{\partial p}{\partial x_i}} \tag{11}$$

The first right-hand side term of Eq. (10) needs closure, typically done as:

$$\overline{V_{k,i}Y_k} - \overline{\rho}(\widetilde{u_i Y_k} - \widetilde{u}_i\widetilde{Y_k}) = \left(-\overline{\rho}\overline{D_k} + \frac{\mu_t}{Sc_k}\right)\frac{\partial \widetilde{Y}_k}{\partial x_i} \tag{12}$$

where μ_t is the turbulent viscosity and Sc_k is the sub-grid scale Schmidt number for species k. The ideal gas equation of state reads $\overline{p} = \overline{\rho}R\widetilde{T}$.

In OpenFOAM, the filtering operation is performed by the grid itself, so only the filter width is specified and not its shape. It is crucial to avoid low-order numerical schemes, as any artificial viscosity that would be added would increase the error and smear out the turbulence [26]. The present study is therefore based on the highest order numerical schemes available within OpenFOAM, namely 2nd-order implicit backward Euler for time derivatives, 2nd-order linear scheme

for the gradient terms, and either 2nd-order linear or 4th-order cubic interpolation for the divergences. Note that the formal spatial accuracy of the cubic interpolation is only second-order. This is due to the treatment of the viscous term that is limited to a linear interpolation. However, since the instabilities in the mixing layer at the flanks of the jet are convective instabilities, the convective terms deliver a higher contribution than the viscous ones. Therefore, it could be expected to obtain an accurate method just by treating only the convective terms with a higher order of accuracy.

There are also many blended schemes available that switch on-the-fly from a high-order to a first-order scheme when the computation encounters strong gradients in the variables, adding numerical viscosity to better deal with the discontinuity and help stability. Indeed, this would be beneficial in resolving shock waves within the near-nozzle. However, for the same aforementioned reason, these methods would not be beneficial in the region further downstream, as they would damp turbulent velocity fluctuations.

The residual or sub-grid scale (SGS) Reynolds stresses $\widetilde{u_i u_j} - \widetilde{u}_i \widetilde{u}_j$ in Eq. (8) require modelling to get the closure of the system. The residual stress tensor reads:

$$\tau_{ij}^{R} = \overline{\rho}(\widetilde{u_i u_j} - \widetilde{u}_i \widetilde{u}_j) \tag{13}$$

with $\overline{\rho}$ being the filtered density. The anisotropic part of the residual stress tensor is defined as [27]:

$$\tau_{ij}^{r} = \tau_{ij}^{R} - \frac{2}{3} k_r \delta_{ij} \tag{14}$$

where k_r denotes the residual kinetic energy $k_r = \frac{1}{2}\tau_{ii}^{R}$. Using a Boussinesq-like hypothesis, the anisotropic contribution of the residual stress tensor is assumed to be directly proportional to the (filtered) strain rate tensor by means of a sub-grid kinematic viscosity ν_{sgs}, namely:

$$\tau_{ij}^{r} = -2\overline{\rho}\nu_{sgs}\widetilde{S}_{ij} \tag{15}$$

where $\widetilde{S}_{ij} = \frac{1}{2}\left(\frac{\partial \widetilde{u}_i}{\partial x_j} + \frac{\partial \widetilde{u}_j}{\partial x_i}\right)$. In this study, three different sub-grid viscosity models will be compared. Smagorinsky was the first to propose an expression for the sub-grid viscosity [28] as:

$$\nu_{sgs} = C_S^2 \Delta^2 \sqrt{2\widetilde{S}_{ij}\widetilde{S}_{ij}} \tag{16}$$

with a model constant $C_S \approx 0.18$ and the filter width $\Delta = (\Delta_x \Delta_y \Delta_z)^{\frac{1}{3}}$. The wall-adapting local eddy-viscosity (WALE) method is another SGS model developed based on the Smagorinsky model [29], where the sub-grid kinematic viscosity is defined as:

$$\nu_{sgs} = C_W^2 \Delta^2 \frac{(S_{ij}^d S_{ij}^d)^{\frac{3}{2}}}{(\widetilde{S}_{ij}\widetilde{S}_{ij})^{\frac{5}{2}} + (S_{ij}^d S_{ij}^d)^{\frac{5}{4}}} \tag{17}$$

where S_{ij}^d is the traceless symmetric part of the square of the velocity gradient tensor. Differently from the Smagorinsky model, this model accounts for both strain and rotational rate of the smallest resolved turbulent scales. As a consequence, most of the turbulent transitional processes and structures relevant for the kinetic energy dissipation are reproduced. The WALE model retains null eddy viscosity in case of a pure shear, which can occur in free jets. It is then possible to reproduce the laminar to turbulent transition process through the growth of linear unstable modes.

There are also models that compute the coefficient appearing in the sub-grid scale viscosity expression on-the-fly as the simulation progresses. While this could improve the accuracy, it certainly increases the computational cost. For instance, the model proposed in Ref. [30] solves an additional transport equation for the sub-grid scale turbulent kinetic energy k_{sgs}:

$$\frac{\partial \overline{\rho} k_{sgs}}{\partial t} + \frac{\partial}{\partial x_i}(\overline{\rho}\widetilde{u}_i k_{sgs}) - \frac{\partial}{\partial x_i}\left[\overline{\rho}(\nu + \nu_{sgs})\frac{\partial k_{sgs}}{\partial x_j}\right] = 2\overline{\rho}\nu_{sgs}\left[\frac{\partial \widetilde{u}_i}{\partial x_j} : \frac{1}{2}\left(\frac{\partial \widetilde{u}_i}{\partial x_j} + \frac{\partial \widetilde{u}_j}{\partial x_i}\right)\right] - \frac{2}{3}\frac{\partial}{\partial x_i}(\overline{\rho}\widetilde{u}_i k_{sgs}) - C_\epsilon \overline{\rho}\frac{k_{sgs}^{3/2}}{\Delta} \tag{18}$$

where the operator ":" denotes the double inner products of two tensors and C_ϵ is a model coefficient derived from local flow properties. The sub-grid scale viscosity is then obtained as

$$\nu_{sgs} = C_k k_{sgs} \Delta \tag{19}$$

with C_k being another model coefficient, whose value again is computed according to local flow attributes. These types of LES models are usually labeled as "one-equation" models. The ability of these eddy-viscosity models to reproduce the near-nozzle region will be investigated in section 4.

2.2. PIMPLE algorithm features for compressible flows

A pressure-based approach within the OpenFOAM framework is used. The solver herein treated is PIMPLE-based, which is a merged PISO-SIMPLE (pressure implicit split operator - semi-implicit method for pressure-linked equations) algorithm. It computes the pressure from momentum and mass conservation, iteratively corrects it, and then updates the density through an equation of state, linking it to the pressure by means of a compressibility factor ψ (for a perfect gas, $\psi = 1/RT$). This is a *segregated* solver: as pressure and velocity are highly coupled in the Nanvier-Stokes equations due to the presence of ∇p in the momentum equations, the mass and momentum equations are solved sequentially in order to decouple them. One way of proceeding in an efficient manner was introduced by Chorin, whose projection method is a fractional step technique in which the velocity is linearised by decomposing it into a solenoidal and an irrotational contribution. The detailed steps of Chorin's method can be found in Ref. [31].

The PIMPLE algorithm [32] is summarised in Fig. 2, where the inner loop refers to the iterations performed to correct the pressure, whereas the outer one denotes how many times the system of equation is solved for a time step. In general, the time step Δt must be set according to a Courant number below 1 to ensure stability, $Co = u\Delta t/\Delta x < 1$, with Δx the grid cell size. This is especially true for PISO-type solvers. PIMPLE algorithms can achieve convergence even for $Co > 1$ [33]. However, such values correspond to a time step whose solution, for highly turbulent LES flows, is far from reality because phenomena with high characteristic velocity are not captured. Accordingly, decreasing the time

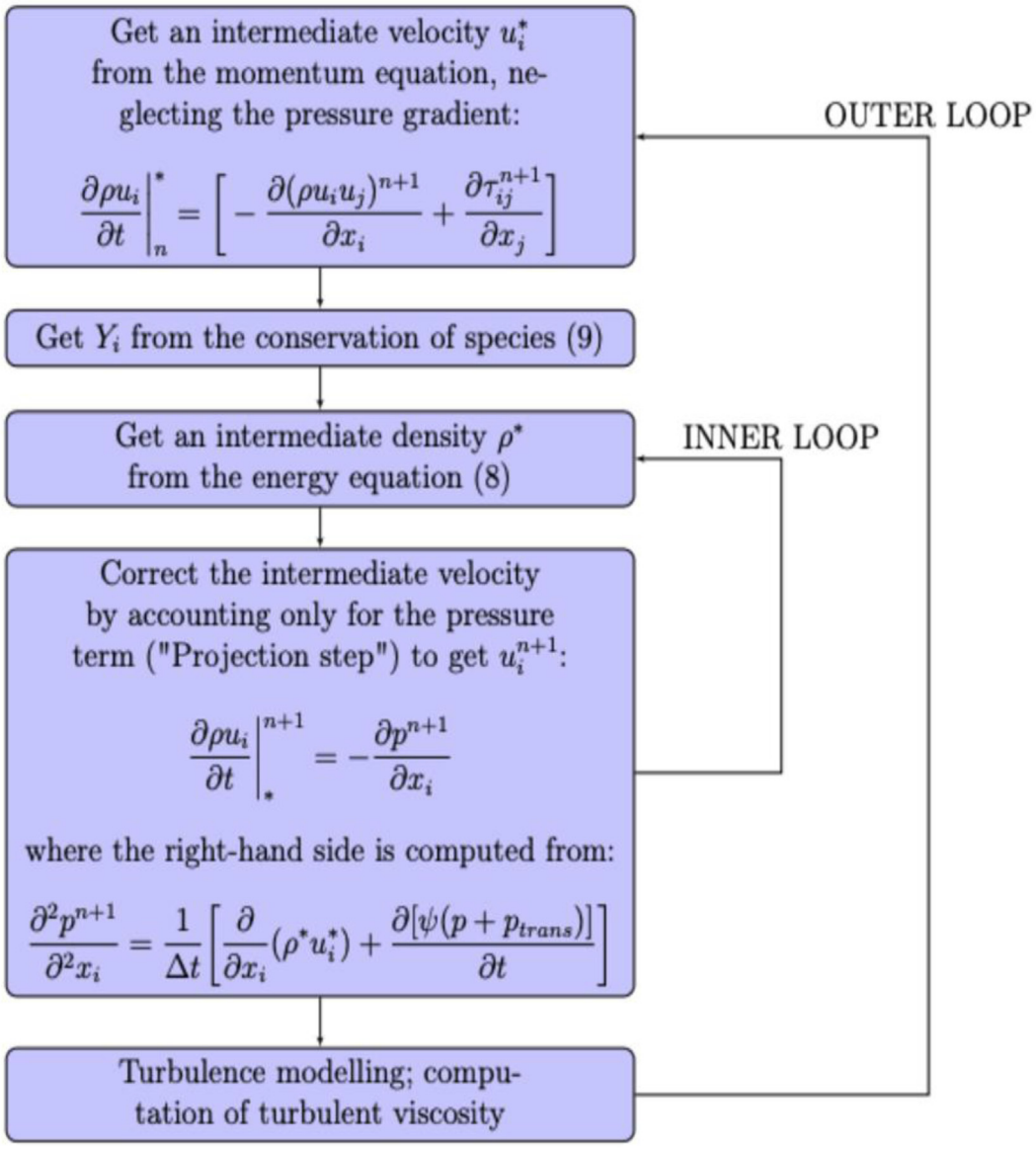

Fig. 2 – Iteration scheme for a single time-step of the PIMPLE algorithm.

step can help capturing more and more turbulent fluctuations. In this sense, a good trade-off between quality of the results and run-time has been found in the present work at $Co = 0.5$.

2.3. *Transonic correction and under-relaxation*

Originally, pressure-based solvers were developed for incompressible and mildly compressible flows, but nowadays they have been extended to account for a broad range of situations, including transonic flows [18,34,35]. The key development has been the reformulation of the pressure equation to include density and velocity correction, ensuring that the type of the equation changed from purely elliptic for incompressible flows to hyperbolic in transonic and supersonic compressible flows [34]. In this way, the pressure plays the dual role of affecting density (through the equation of state) in the limit of high-Mach compressible flow, and velocity (through the gradient in the momentum equation) in the limit of incompressible flow, in order to enforce mass conservation. In particular, the pressure contribution to the density when the flow is compressible reads:

$$\rho_{trans} \approx \left(\frac{\partial \rho}{\partial p}\right)_T p_{trans} = \psi p_{trans} \tag{20}$$

with respect to Fig. 2, within the outer iteration, the sudden change of a certain variable at a certain point in the domain can cause numerical instability. A possible solution is issued by allowing the variable to change only by a fraction α_φ, namely the *under-relaxation* factor. This factor α_φ can be chosen between 0 and 1, where 1 means that no under-relaxation is used.

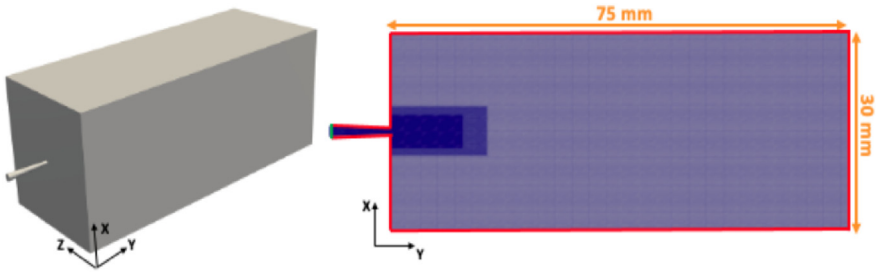

Fig. 3 – Schematic of the computational domain (left) and of the mesh (right, cross section mid-plane) and corresponding boundary conditions (green: inlet, red: walls). (For interpretation of the references to colour in this figure legend, the reader is referred to the Web version of this article.)

3. Computational setup

Simulations of the experimental hydrogen injections in the work of Mansor et al. [36] are performed, in which the jet flows into an argon atmosphere within a cylindrical constant-volume chamber of 8 cm in diameter and 3 cm in depth. For the sake of simplicity, the present domain has been scaled onto a $3 \times 3 \times 7.5$ cm^3 cuboid. In the present work, the nozzle has been placed on the outside and simply shaped as a conical converging body with the same exit diameter of $D = 0.8$ mm as in the experiment. The same is true for the volume of the chamber and the nozzle-wall distance. The boundaries of the geometry (see Fig. 3) consist only of the injection area of the nozzle (the "inlet") and the walls of the injector and combustion chamber (the "walls").

The mesh was inspired by Ref. [13], in which a similar case of injection is investigated, but here adapted in order to achieve a good balance between accuracy and computational speed. After progressive refinements, we came up with the lightest mesh that could convey both stable and reliable computations. It resulted in an almost fully orthogonal grid of (roughly) 5 million cells. However, it has to be noted that it is questionable whether a mesh sensitivity study, in its stricter definition, can be carried out on a large-eddy simulation, since both the discretisation schemes and the sub-grid scale models introduce errors interacting in a non-linear way when changing the grid spacing [37,38].

The largest part of the domain has a cell size of 0.26 mm (D/3). The near-nozzle field features two refinement regions, with cell size of respectively 0.13 mm (D/6) and 0.067 mm (D/12), as depicted in Fig. 3. Smaller cell sizes allow to better capture the thin shock wave discontinuities. Moreover, they reduce the sub-grid scale contribution in the highly shear-generated turbulence zone.

The boundary conditions are summarised in Table 1. The flow is initialized by prescribing a pressure ratio, namely an injection pressure P_0 and an ambient pressure P_∞. The fluid in the domain initially consists of argon and is stagnant everywhere. Following [39], no-slip boundary conditions are applied to all solid walls. The temperature at which the hydrogen is injected is kept fixed at 300 K. The same value sets the initial temperature field in the rest of the domain. The ambient pressure is $P_\infty = 1.2$ MPa as in the experiments. The injection pressure P_0 is varied among 4, 8 and 14 MPa, leading to three different cases with, respectively, NPR = 3.3, 6.7, and 11.7. The computational cost of such simulations translates into approximately 0.02 ms of simulated physical time for every hour of computation, performed on one node and 64 cores, when using static SGS models. When using the dynamic k-equation model, the computational cost increases roughly by 10%.

Table 1 – Boundary and initial conditions.

	Inlet	Walls	Initial field
P [MPa] rowhead	4 - 8 - 14	Zero gradient	1.2
u [m/s] rowhead	-	No-slip	0
T [K] rowhead	300	Zero gradient	300
Y_{H_2} rowhead	1	Zero gradient	0
Y_{Ar} rowhead	0	Zero gradient	1

4. Results

A first overview of the development of the resulting jet in space and time can be found in Fig. 4, where density contours are shown on the two-dimensional mid-plane of the whole chamber. The WALE model has been chosen for the sub-grid scale modelling, together with a 4th-order convective scheme. This combination yields the most reliable results, as will be shown in section 4.4. The hydrogen flow expands from the orifice into the chamber. Due to the strong and sudden injection of gas into a quiescent atmosphere, compression waves surround the jet, reflecting on the walls and then crossing each other. As the injection pressure increases, the jet has a higher H_2 concentration (as indicated by the different colour gradation), a larger width, and a faster penetration.

4.1. *Compressible effects*

As compressibility effects are most challenging for a pressure-based solver, we have a closer look at the near-nozzle field where these phenomena are the strongest. In particular, the effect of under-relaxation on shock resolution has been investigated. In Fig. 5, the simulation results of two identical under-expanded jets at NPR = 3.3, with and without under-relaxation ($\alpha = 0.7$ and $\alpha = 1$, respectively), are compared to Schlieren imaging of a compressed air jet recorded experimentally [40] with a similar pressure ratio (NPR = 5). When under-relaxation is not employed, the

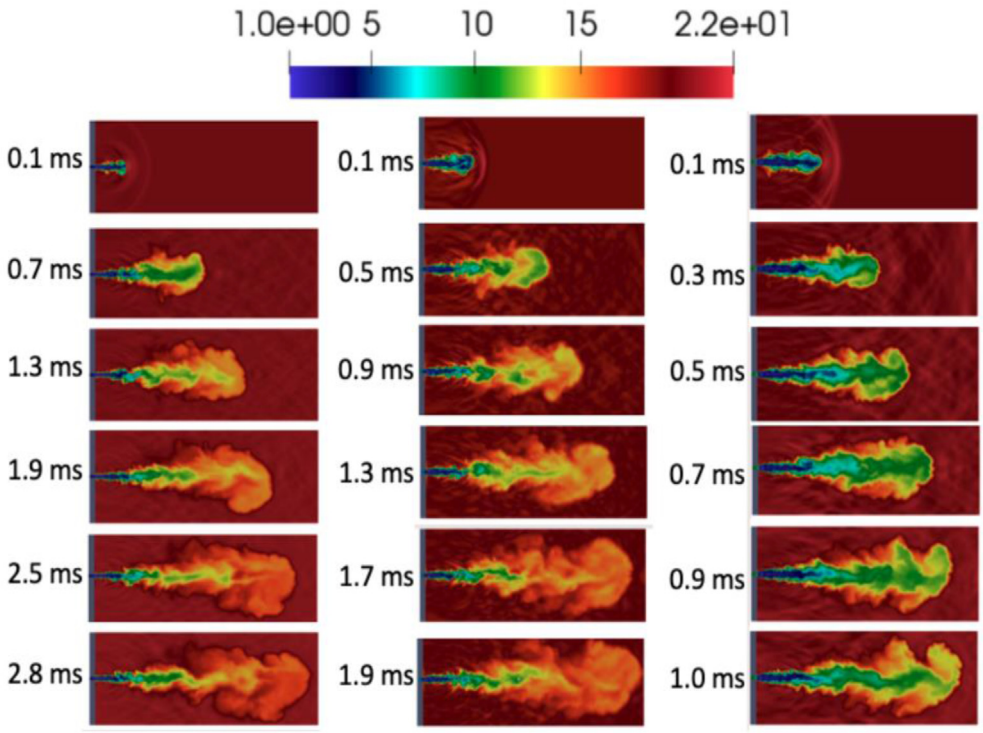

Fig. 4 – Instantaneous density contours (kg/m^3) at the mid-plane at, from left to right respectively, NPR = 3.3, 6.7, and 11.7. Size of the reported area is 30 mm × 75 mm.

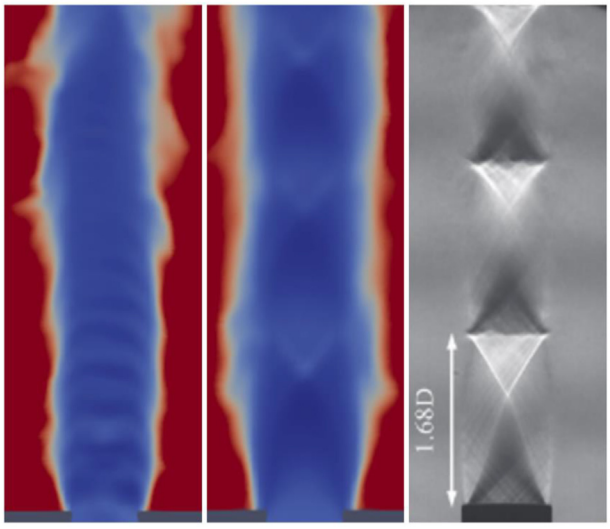

Fig. 5 – Comparison of under-relaxation influence on shock resolution. Left: $\alpha = 1$, middle: $\alpha = 0.7$, right: Schlieren image of air jet at NPR = 5 from Ref. [40].

characteristic shock wave structure is dramatically blurred. Some spurious compression waves can be observed in the nozzle. Taking instead under-relaxation into account allows the pressure-based algorithm at hand to reveal the characteristic diamond pattern at the correct place. The use of high-order discretisation schemes, in particular the 4th-order cubic interpolation that has been applied in our studies, may suffer from spurious oscillations that prevent the convergence of the computations. Even when numerical stability is ensured, under-relaxation factors can help in increasing the accuracy. In Fig. 6 the dependency of the major flow variables on the magnitude of the under-relaxation factor is presented. It is clear that the lower the under-relaxation factor α, the more accurate the shock resolution is. The drawback of a lower α is a slower convergence due to an increased number of required inner iterations [41]. In view of this, one should avoid using too small values of α. A good trade-off between accuracy and efficiency has been found, for the present study, in $\alpha = 0.7$.

4.2. *Mass flow*

The faster jet penetration is a direct consequence of the mass flow exiting the nozzle. The mass flow issued by an injector is the amount of fuel per unit of time that passes through the cross-section area of its nozzle. It is an important quantity as its integral over time denotes how much fuel has been introduced during the injection time. A theoretical estimate of the mass flow exiting a convergent nozzle is provided by the following expression [42]:

$$\dot{m} = A_{nozzle} P_0 \sqrt{\frac{\gamma}{RT_0}} \left(\frac{\gamma+1}{2}\right)^{-\frac{\gamma+1}{2(\gamma-1)}} \tag{21}$$

where A_{nozzle} is the area of the orifice issuing the jet and $\gamma = 1.4$ is the specific heat ratio. It should be noted that, at fixed temperature, $\dot{m}$ depends linearly on the injection pressure only. This behaviour, despite of the isentropic approximation of Eq. (21), is quite well matched by the numerical results in which the mass flow is directly computed from the density

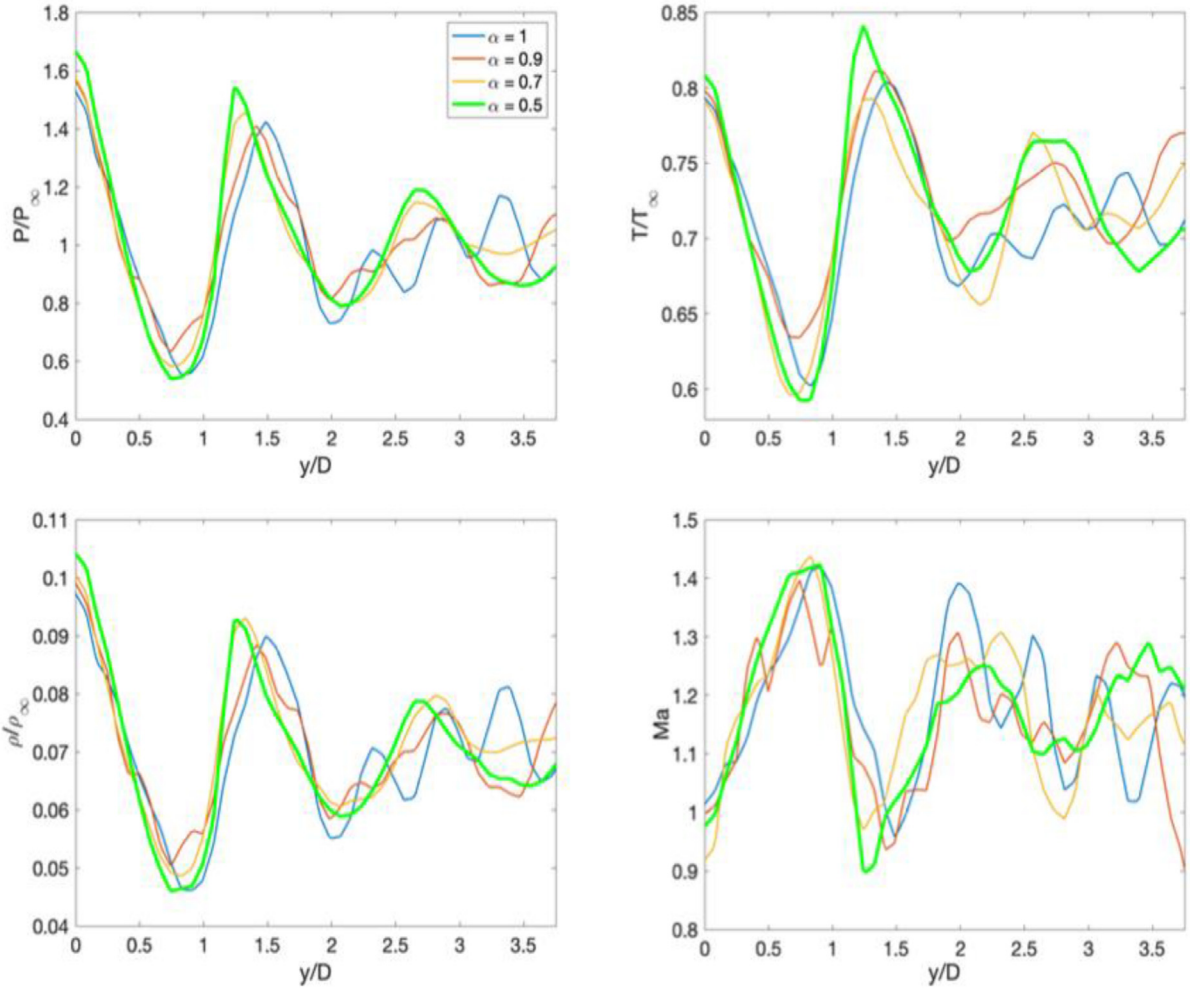

Fig. 6 – Near-orifice pressure, temperature, density and Mach number as function of the axial distance along the centerline at different under-relaxation factors.

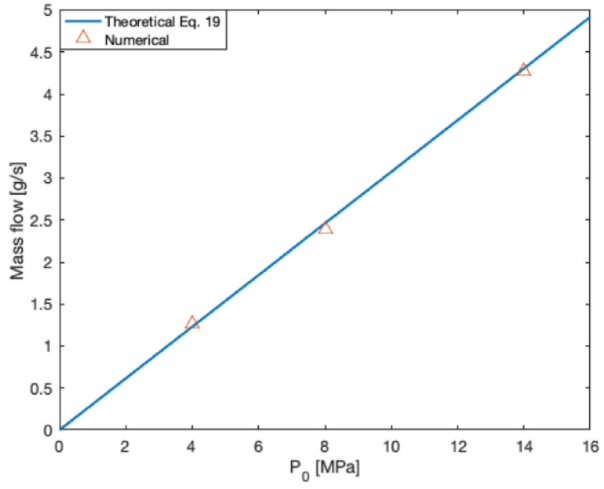

Fig. 7 – Computed and theoretical nozzle mass flows for different injection pressures.

and velocity field, as shown in Fig. 7. Not only is the trend of mass flow versus injection pressure linear, but also the computed mass flow values resemble with good accuracy the ones estimated by Eq. (21). This means that the discharge coefficient of the simulation is approximately 1, i.e. an ideal situation where no pressure head losses occur within the nozzle. Unfortunately, the experimental mass flows are not reported in Ref. [36].

4.3. *Cone angle*

As well as the penetration, the radial spreading of the jet gets larger with increasing NPR. These two aspects are connected by mass and momentum conservation. Simply speaking, the more the jet diffuses laterally, the less mass and momentum is available to penetrate in the axial direction, and vice versa. From an experimental point of view, this is typically measured by means of the cone angle, i.e. the angle between the jet boundaries. There are various methods to measure it [43]. Here, we choose to compute the angle from the jet's equivalent area [44–46], and compare them to the ones measured

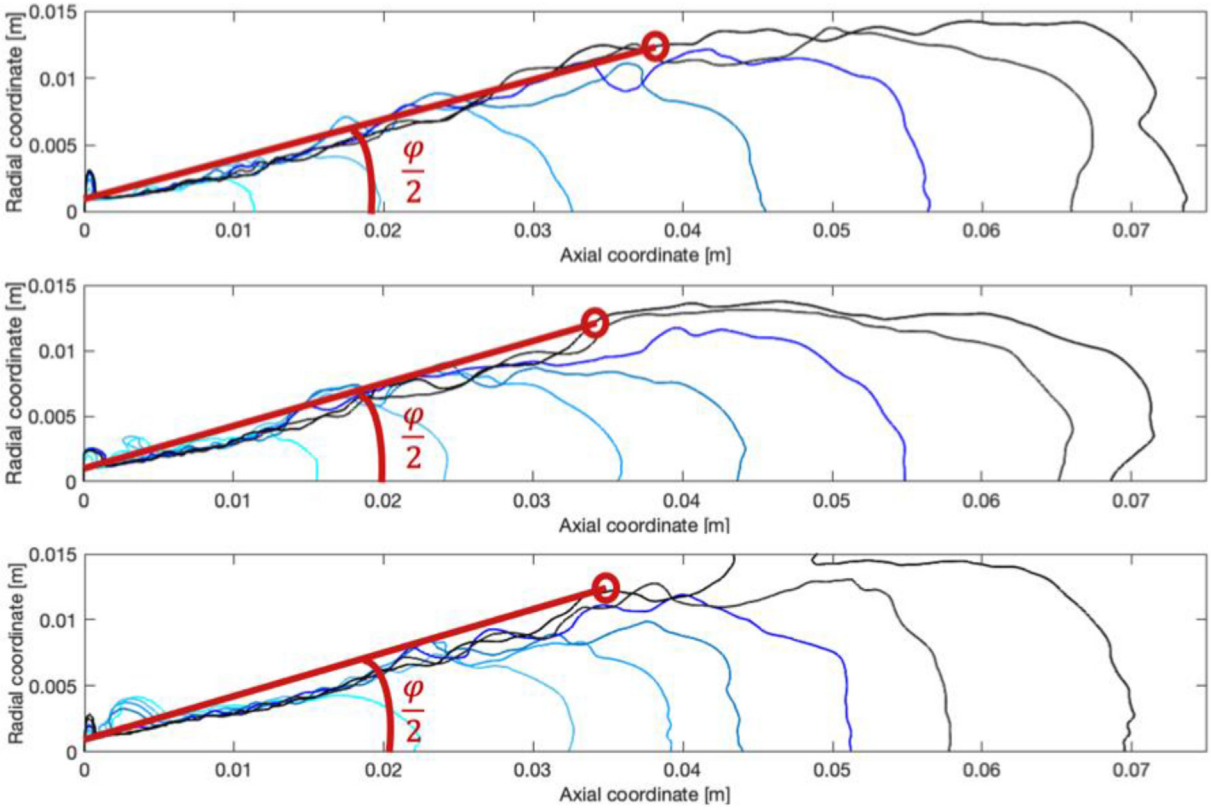

Fig. 8 – Cone angle of hydrogen jets at, from above to bottom, NPR = 3.3, 6.7, 11.7. The measurements have been performed by computing the angle swept by the equivalent jet triangle area at y = L/2 and Y_{H_2} = 0.001

experimentally by Ref. [36]. In order to do so, the flow has been first circumferentially averaged. The corresponding results are shown in Fig. 8 and in Table 2. The first thing to notice is that, in the same fashion as for the experimental reference, the computed angles increase with increasing NPR. This correct trend confirms the solidity of the numerical approach. When the individual cases are compared, there is a discrepancy of 3–6°. These differences may be attributed to the uncertainty in the angle measurements. In fact, locating the jet boundaries is challenging. It depends strongly on the threshold used to identify it [47], and it can reach an uncertainty up to 24% [48]. Here, we decided to represent the jet by the isocontour corresponding to the 0.1% H_2 mass fraction (i.e. Y_{H_2} = 0.001, using the same definition used for the jet tip penetration in 4.4), but a unique definition on where to measure the jet angle is not present in literature. To underline the sensitivity of the angle computation, we report also in Table 2 the angle calculated when taking the hydrogen mass fraction equal to 0.2%. Indeed, when 0.2 is chosen as threshold, the computed angles are 2–3° smaller, and closer to the ones predicted experimentally.

Table 2 – Computed cone angles φ and comparison with the experimental values of [36] for different injection pressures. Two different threshold criteria, 0.1% and 0.2% hydrogen mass fraction, have been used to highlight the sensitivity of the measurement.

P_0	NPR	Y_{H2} = 0.1%	Y_{H2} = 0.2%	Exp [36].
4 MPa	3.3	29.4°	27.3°	22.9°
8 MPa	6.7	32.0°	28.8°	26.4°
14 MPa	11.7	35.2°	33.0°	31.0°

4.4. *Jet penetration*

The jet tip penetration is one of the key parameters that characterise under-expanded jets with regards to air-fuel mixing and mixture formation in direct injection engines [49]. The penetration has been determined in this study by recording the axial distance from the nozzle exit to the position where the mass fraction of hydrogen falls below a threshold of 0.1%, as introduced by Ref. [44]. In under-expanded flows with Reynolds number in the order of 10^5 – 10^6, as in the present work, such measure of penetration length was found to be a linear function of the square root of time [50]. This behaviour is encountered as well in our study, as can be observed in Fig. 9, where the experimental data from Ref. [36] are compared to the theoretical trend and to the results coming from our simulations for three different injection pressures. The trends of the numerical simulations follow the experimental ones and fit the linear trend, confirming the validity of the present numerical model. The jet has a high velocity immediately after the nozzle, then it starts decelerating and spreading radially due to loss of momentum. As the NPR increases, the jet tip penetration rate increases due to higher momentum, hence resulting in a faster flow.

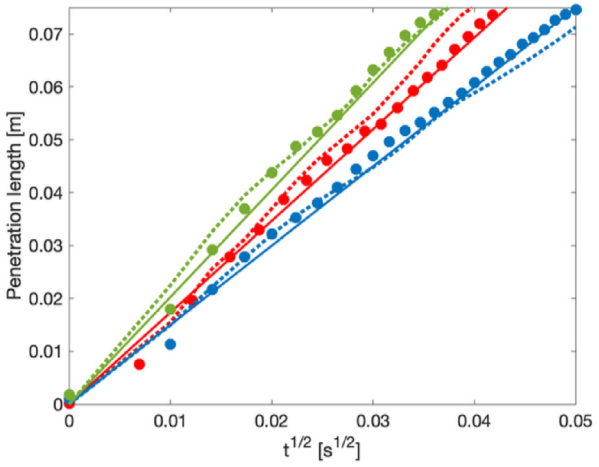

Fig. 9 – Jet penetration length as a function of the square root of time. Blue: NPR = 3.3, red: NPR = 6.7, green: NPR = 11.7. Circles: experimental data, dashed lines: present study, solid lines: theoretical trend. (For interpretation of the references to colour in this figure legend, the reader is referred to the Web version of this article.)

The penetration lengths of hydrogen are reported for the three different injection pressures, computed with different combinations of LES models and convective discretisation schemes. First, the static Smagorinsky and WALE models and the dynamic k-equation model are compared in Fig. 10. It can be seen that the penetration curves on overall are quite similar. One thing worth underlining is that the error accumulates in time. This is why the differences among the LES models are larger when the NPR is lower, i.e. when the jet is slower. In the initial development of the jet the Smagorinsky model predicts a deeper penetration in time. Indeed, the Smagorinsky model is not suitable for high shear flows, since the SGS dissipation is too high to correctly predict the transition to turbulence during the initial evolution of the jet, resulting in a substantial underprediction of jet width [51] and over-prediction of jet penetration. The dynamic K-equation model appears most accurate for high NPR values but lacks precision with respect to the expected trend in the case with NPR = 3.3. On the contrary, the static WALE model matches the experimental data on average better.

In Fig. 11, the WALE model is then compared to the dynamic K-equation model with different discretisation schemes. When coupled with the linear scheme, the results get closer to the reference data when NPR = 11.7, and the same is true with cubic interpolation when NPR = 6.7, whereas for NPR = 3.3 there is little difference between the two discretisation schemes. In general, one would prefer the cubic scheme over the linear interpolation due to the higher order of accuracy in the convective terms, and hence improved description of the turbulence.

In order to reduce the statistical uncertainty, one should in principle average an ensemble of as many different turbulent realisations as possible [52]. Simulation has to be

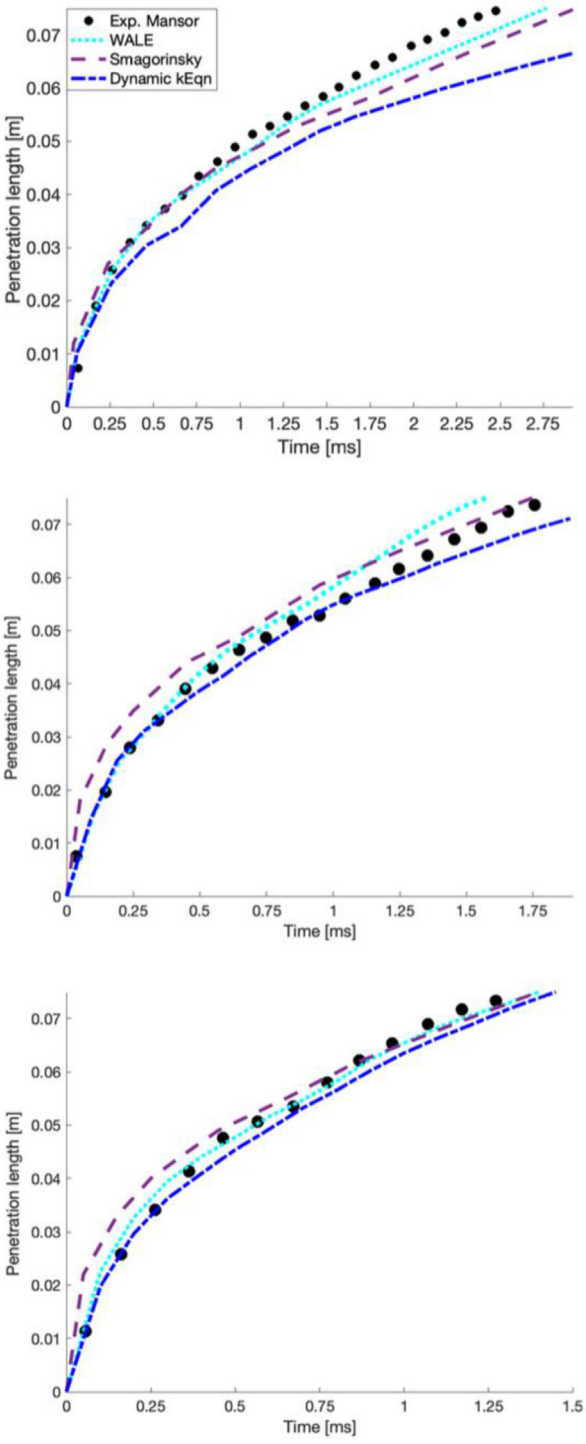

Fig. 10 – H_2 penetration length at different NPR values (top: NPR = 3.3, middle: NPR = 6.7, bottom: NPR = 11.7) with different SGS models.

repeated many times, requiring a high computational effort. However, there could be cases in which this operation would add little information, for instance, in high-velocity strong shear flows where most of the turbulence is generated by the development of the jet rather than influenced by the initial turbulent conditions. In order to investigate this, additional

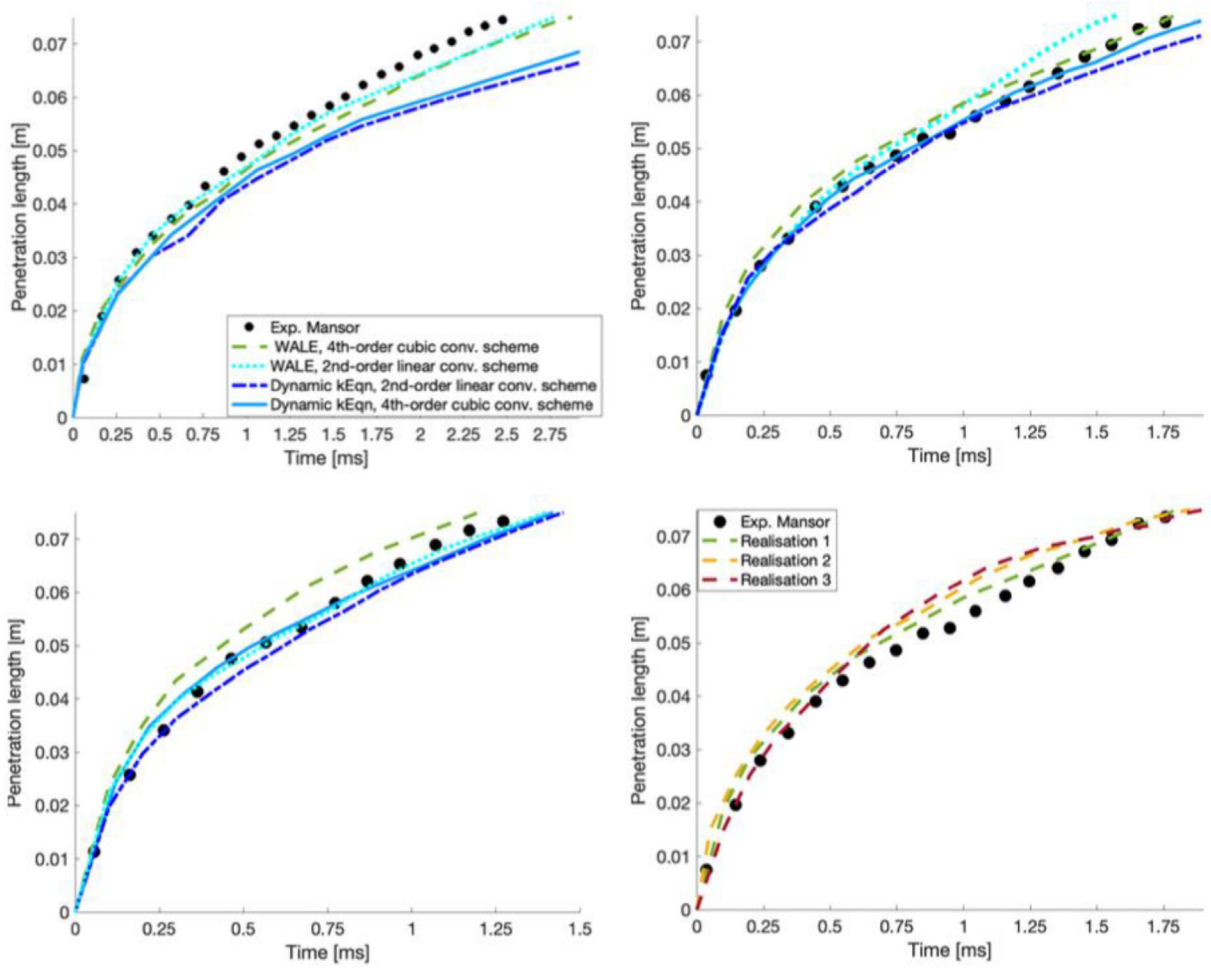

Fig. 11 – H_2 penetration length at different NPR values with different LES models and convective schemes. Top left: NPR = 3.3, top right: NPR = 6.7, bottom left: NPR = 11.7. The bottom right panel shows results for different turbulent realisations (NPR = 11.7).

simulations of the NPR = 6.7 case have been performed, for which some turbulent white noise has been prescribed constantly in time at the inlet of the nozzle, in order to introduce a certain amount of random fluctuations to the flow along the three directions in space. More precisely, a digital-filter based inlet boundary condition for velocity is used to generate synthetic turbulence-alike time-series, where the root mean squared (RMS) fluctuation scale is 10% of the mean flow in every direction in space. The bottom-right panel of Fig. 11 shows the jet penetration in time for three different realisations: one with no added turbulence at the inlet, and two additional simulations with the same turbulence intensity prescribed at the inlet but with different randomness. It can be noted that the jet penetration length does not differ too much from one simulation to the other, at most 5%, compared to the maximum difference that characterises the single realisations with different LES models and numerical schemes, that can reach values up to 20%. We can then conclude that differences much bigger than 5% are not due to a particular realisation but rather to the method used. Hence, one single realisation is deemed here sufficient to fully characterise the jet.

5. Conclusions

In the present paper, the suitability of a pressure-based PIMPLE-solver for large-eddy simulation of non-reactive, under-expanded, highly turbulent H_2 jets for engine applications has been investigated for the first time. The advantage of using such a solver is to keep a high accuracy in describing the low-Mach turbulence occurring in most of the domain, meanwhile being still able to capture fairly well, through a proper transonic correction, the strong compressible discontinuities that arise in the near-orifice field. To this end, it is shown that the use of under-relaxation factors improves the shock resolution, especially when oscillatory high-order interpolation schemes are employed. Different LES models and numerical schemes have then been assessed. The static Smagorinsky model appears to be unsuitable for the investigated flows. The dynamic K-equation model looks to be more accurate for high injection pressure but lacks precision for the case with low NPR. In the end, the WALE model with 4th-order convective schemes has been found to be the best trade-off between accuracy and computational time, and hence it is

the recommended choice for this specific case. Since the results coming from different turbulent realisations are very similar, it is shown that one realisation is sufficient to fully characterise the jet.

Describing the fuel mixing with the surrounding environment in a correct way is fundamental in view of incorporating combustion modelling. Hence, such a study is of importance from a practical perspective, constituting a solid step towards clean combustion of hydrogen for DI-CI engine applications. The pressure-based model investigated in the present manuscript has the advantage of describing both the high-Ma compressible discontinuities and low-Ma turbulence, in particular the ones arising in high-pressure hydrogen jets, with acceptable accuracy and a high computational efficiency.

Declaration of competing interest

The authors declare that they have no known competing financial interests or personal relationships that could have appeared to influence the work reported in this paper.

Acknowledgements

This publication is part of the Argon Power Cycle project (project number 17868) financed by the Dutch Research Council (NWO).

REFERENCES

[1] Pugazhendhi A, Chen W-H. Hydrogen energy technology for future. Int J Hydrogen Energy 2022;47:37153.
[2] Marchenko O, Solomin S. The future energy: hydrogen versus electricity. Int J Hydrogen Energy 2015;40:3801–5.
[3] Adeel A, Abul A-A, Angelina A, Saidur R. Hydrogen fuel and transport system: a sustainable and environmental future. Int J Hydrogen Energy 2016;41:1369–80.
[4] Rana K, N DS, Jilakara S. Potential of hydrogen fuelled ic engine to achieve the future performance and emission norms. SAE Technical Papers; 2015.
[5] Yip HL, Srna A, Yuen ACY, Kook S, Taylor RA, Yeoh GH, Medwell PR, Chan QN. A review of hydrogen direct injection for internal combustion engines: towards carbon-free combustion. Appl Sci 2019;9.
[6] Onorati A, Payri R, Vaglieco B, Agarwal A, Bae C, Bruneaux G, Canakci M, Gavaises M, Günthner M, Hasse C, Kokjohn S, Kong S-C, Moriyoshi Y, Novella R, Pesyridis A, Reitz R, Ryan T, Wagner R, Zhao H. The role of hydrogen for future internal combustion engines. Int J Engine Res 2022:529–40.
[7] Ogden JM. Hydrogen: the fuel of the future? Phys Today 2002;55:69–75.
[8] Oh S, Kim C, Lee Y, Yoon S, Lee J, Kim J. Experimental investigation of the hydrogen-rich offgas spark ignition engine under the various compression ratios. Energy Conversion and Management; 2019.
[9] Kim J, Chun KM, Song S, Baek H-K, Lee SW. Hydrogen effects on the combustion stability, performance and emissions of a turbo gasoline direct injection engine in various air/fuel ratios. Applied Energy; 2018.
[10] Kee S-S, Shioji M, Mohammadi A, Nishi M, Inoue Y. Knock characteristics and their control with hydrogen injection using a rapid compression/expansion machine. SAE Trans 2007;116:217–26.
[11] Song J, Park S. Combustion characteristics of a methane engine with air- and n2-assisted direct injection. Fuel; 2017.
[12] Lee S, Kim G, Bae C. Behavior of hydrogen hollow-cone spray depending on the ambient pressure. Int J Hydrogen Energy 2021;46:4538–54.
[13] Hamzehloo A, Aleiferis P. Computational study of hydrogen direct injection for internal combustion engines. SAE Technical Papers 2013;11.
[14] Vuorinen V, Yu J, Tirunagari S, Kaario O, Larmi M, Duwig C, et al. Large-eddy simulation of highly underexpanded transient gas jets. Phys Fluids 2013;25:016101.
[15] Li X, Wu K, Yao W, Fan X. A comparative study of highly underexpanded nitrogen and hydrogen jets using large eddy simulation. Int J Hydrogen Energy 2016;41:5151–61.
[16] Duronio F, Montanaro A, Ranieri S, Allocca L, De Vita A. Under-expanded jets characterization by means of cfd numerical simulation using an open foam density-based solver. In: 15th international conference on engines & vehicles. SAE International; 2021.
[17] Bonelli F, Viggiano A, Magi V. A numerical analysis of hydrogen underexpanded jets under real gas assumption. J Fluid Eng 2013;135.
[18] Zhang L, Kumbaro A, Ghidaglia J-M. A conservative pressure based solver with collo- cated variables on unstructured grids for two-fluid flows with phase change. J Comput Phys 2019:265–89.
[19] Lai Y, So R, Przekwas A. Turbulent transonic flow simulation using a pressure-based method. Int J Eng Sci 1995;33:469–83.
[20] Miettinen A, Siikonen T. Application of pressure- and density-based methods for different flow speeds. Int J Numer Methods Fluid 2015;79:243–67.
[21] Li X, Chen Q, Chen M, He Q, Christopher DM, Cheng X, Chowdhury BR, Hecht ES. Modeling of underexpanded hydrogen jets through square and rectangular slot nozzles. Int J Hydrogen Energy 2019;44:6353–65.
[22] Babayev R, Andersson A, Dalmau AS, Im HG, Johansson B. Computational optimization of a hydrogen direct-injection compression-ignition engine for jet mixing dominated nonpremixed combustion. Int J Engine Res 2022;23:754–68.
[23] Rutland CJ. Large-eddy simulations for internal combustion engines – a review. Int J Engine Res 2011;12:421–51.
[24] Poinsot T, Veynante D. Theoretical and numerical combustion. R.T. Edwards; 2005.
[25] Khaksarfard R, Kameshki M, Paraschivoiu M. Numerical simulation of high pressure release and dispersion of hydrogen into air with real gas model. Shock Waves 2010:205–16.
[26] Roos Launchbury D. Recommendations for LES simulations. Wiesbaden: Springer Fachmedien Wiesbaden; 2016. p. 63–8.
[27] Pope SB. Turbulent flows. Cambridge University Press; 2000.
[28] Smagorinsky J. General circulation experiments with the primitive equations. i. the basic experiment. Mon Weath 1963;91:99–164.
[29] Franck N, Ducros F. Subgrid-scale stress modelling based on the square of the velocity gradient tensor. Flow, Turbul Combust 1999;62:183–200.
[30] Kim W-W, Menon S. A new dynamic one-equation subgrid-scale model for large eddy simulations. 33rd Aerospace Sciences Meeting and Exhibit; 1995.
[31] Chorin AJ. Numerical solution of the Navier-Stokes equations. Math Comput 1968;22:745–62.

[32] Ferziger JH, Perić M. Computational methods for fluid dynamics. 2nd ed. Berlin: Springer; 1999.
[33] Aravind Karthik M, Srinivas G, Naik N. Implementation of higher-order pimple algorithm for time marching analysis of transonic wing compressibility effects with high mach pre-conditioning. Engineered Science 2022;20:218–35.
[34] Karki KC, Patankar SV. Pressure based calculation procedure for viscous flows at all speedsin arbitrary configurations. AIAA Journal 1989;27:1167–74.
[35] Harlow FH, Amsden AA. A numerical fluid dynamics calculation method for all flow speeds. J Comput Phys 1971;8:197–213.
[36] Mansor MRA, Nakao S, Nakagami K, Shioji M. Study on hydrogen-jet development in the argon atmosphere. Green Energy and Technology Zero-Carbon Energy Kyoto; 2012. p. 177–84.
[37] Kempf A, Geurts B, Oefelein J. Error analysis of large-eddy simulation of the turbulent non-premixed sydney bluff-body flame. Combustion and Flame; 2011.
[38] Salvetti M, Meldi M, Luca B, Sagaut P. Reliability of large-eddy simulations: benchmarking and uncertainty quantification. ERCOFTAC Series 2018:15–23.
[39] Gad-el Hak M. The fluid mechanics of microdevices—the freeman scholar lecture. J Fluid Eng 1999;121:5–33.
[40] Wei X, Mariani R, Chua L, Lim H, Lu Z, Cui Y, New T. Mitigation of under-expanded supersonic jet noise through stepped nozzles. J Sound Vib 2019;459:114875.
[41] Barron RM, Salehi Neyshabouri AA. Effects of under-relaxation factors on turbulent flow simulations. Int J Numer Methods Fluid 2003;42:923–8.
[42] Dong C, Cui X, Liu S, Jiang Z, Wu Y. Investigation on the choked mass-flow characteristics of the helium fluid during the joule-thomson process in micro-orifice under different high pressures. Cryogenics 2022;122:103416.
[43] Ruiz-Rodriguez I, Pos R, Megaritis T, Ganippa L. Investigation of spray angle measurement techniques. IEEE Access; 2019. p. 1. 1.
[44] Naber JD, Siebers DL. Effects of gas density and vaporization on penetration and dispersion of diesel sprays. SAE Technical Paper; 1996.
[45] Payri F, Payri R, Bardi M, Carreres M. Engine combustion network: influence of the gas properties on the spray penetration and spreading angle. Exp Therm Fluid Sci 2014;53:236–43.
[46] Emberson D, Ihracska B, Imran S, Diez A. Optical characterization of diesel and water emulsion fuel injection sprays using shadowgraphy. Fuel 2016;172:253–62.
[47] Canny J. A variational approach to edge detection. In: Proceedings of the third AAAI conference on artificial intelligence, AAAI'83. AAAI Press; 1983. p. 54–8.
[48] Macian V, Payri R, Garcia A, Bardi M. Experimental evaluation of the best approach for diesel spray images segmentation. Exp Tech 2012;36:26–34.
[49] Yu J, Vuorinen V, Kaario O, Sarjovaara T, Larmi M. Characteristics of high pressure jets for direct injection gas engine. SAE Int J Fuels Lubricants 2013;6:149–56.
[50] Petersen B, Ghandhi J. Transient high-pressure hydrogen jet measurements. SAE 2006 World Congress & Exhibition; 2006.
[51] Le Ribault C, Sarkar S, Stanley SA. Large eddy simulation of a plane jet. Phys Fluids 1999;11:3069–83.
[52] Farrace D, Panier R, Schmitt M, Boulouchos K, Wright YM. Analysis of averaging methods for large eddy simulations of diesel sprays. SAE Int J Fuels Lubricants 2015;8:568–80.